

Ferroelectric-tuned van der Waals heterojunction with band alignment evolution

Yan Chen

National Laboratory for Infrared Physics, Shanghai Institute of Technical Physics, Chinese Academy of Science, Shanghai, 200083

Xudong Wang

Shanghai Institute of Technical Physics, Chinese Academy of Sciences

Le Huang

Guangdong University of Technology

Xiaoting Wang

Institute of Semiconductors, Chinese Academy of Sciences

Wei Jiang

Shanghai Institute of Technical Physics, Chinese Academy of Sciences

Zhen Wang

Chinese Academy of Science

Peng Wang

Shanghai Institute of Technical Physics, Chinese Academy of Sciences

Binmin Wu

Shanghai Institute of Technical Physics, Chinese Academy of Sciences

Tie Lin

Shanghai Institute of Technical Physics, Chinese Academy of Sciences

Hong Shen

Shanghai Institute of Technical Physics, Chinese Academy of Sciences <https://orcid.org/0000-0001-6283-6506>

Zhongming Wei

Institute of Semiconductors, Chinese Academy of Sciences <https://orcid.org/0000-0002-6237-0993>

Weida Hu

Shanghai Institute of Technical Physics, Chinese Academy of Sciences <https://orcid.org/0000-0001-5278-8969>

Xiangjian Meng

National Laboratory for Infrared Physics, Shanghai Institute of Technical Physics, Chinese Academy of Sciences

Junhao Chu

Fudan University

Jianlu Wang ([✉ jlwang@mail.sitp.ac.cn](mailto:jlwang@mail.sitp.ac.cn))

Article

Keywords: Van der Waals (vdW) integration, devices, band alignment evolution

Posted Date: January 7th, 2021

DOI: <https://doi.org/10.21203/rs.3.rs-134208/v1>

License:  This work is licensed under a Creative Commons Attribution 4.0 International License.

[Read Full License](#)

Version of Record: A version of this preprint was published at Nature Communications on June 29th, 2021. See the published version at <https://doi.org/10.1038/s41467-021-24296-1>.

1 **Ferroelectric-tuned van der Waals heterojunction with band
2 alignment evolution**

3 Yan Chen^{1,2#}, Xudong Wang^{1#}, Le Huang³, Xiaoting Wang³, Wei Jiang¹, Zhen Wang¹,
4 Peng Wang¹, Binmin Wu¹, Tie Lin¹, Hong Shen¹, Zhongming Wei^{3*}, Weida Hu^{1,4*},
5 Xiangjian Meng¹, Junhao Chu^{1,2}, Jianlu Wang^{1,4*}

6 ¹*State Key Laboratory of Infrared Physics, Shanghai Institute of Technical Physics,
7 Chinese Academy of Sciences, 500 Yu Tian Road, Shanghai 200083, China.*

8 ²*School of Physics and Electronic Science, East China Normal University, Shanghai
9 200241, China.*

10 ³*State Key Laboratory of Superlattices and Microstructures, Institute of
11 Semiconductors, Chinese Academy of Sciences, Beijing 100083, China*

12 ⁴*Hangzhou Institute for Advanced Study, University of Chinese Academy of Sciences,
13 Chinese Academy of Sciences, Hangzhou 310024, China*

14 *Corresponding authors:

15 Jianlu Wang (email: jlwang@mail.sitp.ac.cn)

16 Weida Hu (email: wdhu@mail.sitp.ac.cn)

17 Zhongming Wei (email: zmwei@semi.ac.cn)

18 [#]These authors contributed equally: Yan Chen, Xudong Wang.

19

1 Van der Waals (vdW) integration with abundant two-dimensional materials
2 provides a broad basis for assembling functional devices. However, band
3 alignment in a specific vdW heterojunction (VHJ) is difficult to tune, restricting
4 its multifunctionality and structural simplicity. Here, we designed a ferroelectric-
5 tuned VHJ (Fe-VHJ) device structure by integrating a GeSe/MoS₂ VHJ and poly
6 (vinylidene fluoride-trifluoroethylene) (P(VDF-TrFE))-based ferroelectric
7 polymer. An ultrahigh electric field derived from the ferroelectric polarization
8 that can effectively modulate the band alignment of the GeSe/MoS₂ heterojunction.
9 Band alignment transition of the heterojunction from type II to type I was
10 demonstrated. The combination of anisotropic GeSe with MoS₂ realised a high-
11 performance polarization-sensitive photodetector exhibiting low dark current of
12 approximately 1.5 pA, quick response of 14 μs, and high detectivity (D^*) of $4.7 \times$
13 10^{13} Jones. Dichroism ratios were also enhanced by ferroelectric polarization in a
14 broad-spectrum from visible to near-infrared. The GeSe/MoS₂ Fe-VHJ has great
15 potential for multifunctional detection applications in sophisticated light
16 information sensing. More profoundly, the Fe-VHJ structure provides a valid
17 band-engineering approach to creating versatile devices.

18

1 Heterojunctions are an essential part of functional devices. The integration of
2 different materials guarantees the acquisition of high-performance heterojunctions.
3 Traditional integration strategies, such as chemical and physical epitaxial growth,
4 commonly require harsh preparation conditions and rarely achieve the ideal interface.
5 Interface disorder, chemical contamination, strain, and diffusion effects limit the
6 performance and application of heterostructures.¹⁻³ Emerging two-dimensional (2D)
7 layered materials provide a state-of-the-art approach to designing heterojunctions based
8 on van der Waals (vdW) interaction. A vdW heterojunction (VHJ) is bond-free
9 integration that is unaffected by the lattice mismatch or the processing condition of
10 materials used. As basic building blocks, various 2D materials exhibit impressive
11 electrical, optical, and magnetic properties.⁴⁻⁶ Moreover, vdW integration with an
12 atomically clean surface in the heterostructure that is notably superior to those of only
13 one material.^{7,8} An excellent example is the twisted integration of two monolayer
14 graphene that exhibit unconventional superconductivity and correlated insulator
15 behaviour.^{9,10} In addition to fundamental physics research, studies have reported that
16 VHJs have excellent potential in high-performance multifunctional devices.
17 Optoelectronic devices, such as photovoltaic photodetectors^{11,12} and quantum well
18 LEDs,¹³ have attracted tremendous research interest because they exhibit remarkably
19 better performance than traditional devices. Electronic devices such as floating-gate
20 memories^{14,15} and tunnelling diodes¹⁶⁻¹⁸ have exhibited great potential for future
21 applications as well.

22 With band structure design, the richness of 2D materials and the flexibility of vdW
23 integration provide numerous routes to realise specific functional devices. Typically,
24 three different band alignments can be formed in VHJs, but multi-functional
25 applications are challenging to achieve with a fixed band alignment. Reliable
26 approaches to engineering the band structure in VHJs should be explored. External
27 fields, commonly an electric field supplied by a gate voltage, have been extensively
28 explored to tune the band structure and yield additional properties and functions in the
29 VHJ.¹⁹ Woo Jong Yu *et al.* used an external gate to modulate the band slope and

1 photocurrent generation of graphene-MoS₂-graphene vertical heterostructure with high
2 quantum efficiency.¹² High-performance BP/MoS₂ VHJ realized tunable
3 multifunctional operations by shifting the band-structure alignment across the
4 heterojunction.²⁰ By sufficient controlling of an external electric field, VHJs can
5 achieve robust performance and expand diverse application potentials.

6 However, tuning of the Fermi levels by the electric field is insufficient to change
7 the band offset, which affects the performance of a heterojunction significantly. Besides,
8 a sustained external voltage to maintain the optimal performance of the device causes
9 considerable power consumption. Ferroelectrics provide a non-volatile remanent
10 polarization electric field over 1 V/nm,²¹⁻²³ which is large enough to modify the
11 bandgap of semiconductors according to the Stark effect.²⁴⁻²⁷ Ferroelectric field-effect
12 transistors based on ferroelectrics and 2D materials have been demonstrated high
13 performances and great potentials in electronics and optoelectronics.²⁸⁻³⁰ Predictably,
14 combining ferroelectrics with VHJs achieves highly tunable band structures and
15 tailored optoelectronic properties. Here, we designed a ferroelectric VHJ (Fe-VHJ)
16 consisting of a ferroelectric polymer, P(VDF-TrFE), and GeSe/MoS₂ VHJ. Under
17 modulation of the ferroelectric polarization field, the electrical characteristics of the
18 GeSe/MoS₂ *pn* junction can be tuned and its output can be maintained at two specific
19 states. The band alignment between GeSe and MoS₂ can be switched from type II
20 (staggered) to type I (straddling) by reversing the direction of ferroelectric polarization
21 field. With ferroelectric-tuned VHJ band engineering, the GeSe/MoS₂ junction can act
22 as a high-performance photodetector. High responsivities are achieved for a wide range
23 of wavelengths spanning from visible to near-infrared. The anisotropy of GeSe is
24 employed to demonstrate a polarized light-sensitive photodetector, which is further
25 enhanced by the ferroelectric field. More importantly, the ferroelectric field is applied
26 on the VHJ to engineer the band alignment type, broaden the detection wavelength
27 range, and enrich functionalities.

28

29 **Fabrication of GeSe/MoS₂ Fe-VHJ**

1 The device structure we designed is depicted in **Fig. 1a**. GeSe and MoS₂ form the
2 VHJ, in which GeSe is an anisotropic 2D semiconductor. Unlike MoS₂, which has an
3 in-plane hexagonal structure, GeSe has a rectangular structure in the plane, that is,
4 different structures in the x and y directions. It has an ‘armchair’ shape along the x-axis
5 and a ‘zigzag’ shape along the y-axis. The specific atomic structure of GeSe is
6 illustrated in Supplementary Fig. 1. Because of its anisotropic structure, GeSe possesses
7 electrical anisotropy and optical linear dichroism, which satisfies its application in
8 polarized light detection. P(VDF-TrFE) is covered on the GeSe/MoS₂ VHJ. Here we
9 apply it to engineer the band structure and enhance the optoelectronic performance of
10 the VHJ. The band structure of GeSe and MoS₂ is shown in **Fig. 1b**. The bottom of the
11 conduction band and the top of the valence band of GeSe (MoS₂) are approximately
12 −4.1 eV (−4.2 eV) and −5.2 eV (−5.4 eV).³¹ The offsets of the conduction band and
13 valence band are approximately 0.1 eV and 0.2 eV, respectively. Therefore, a type II
14 band alignment is formed, which is beneficial for separating photo-generated carriers
15 and achieving high-speed photoresponse. **Figure 1c** is an optical micrograph of the
16 device. Electrodes are situated near the boundary of the overlapped heterojunction to
17 eliminate the effect of series resistance. The heterostructure composed of GeSe and
18 MoS₂ is well-assembled, as confirmed by Raman spectra and transmission electron
19 microscopy (TEM). As shown in **Fig. 1d**, the heterostructure exhibits Raman
20 characteristic peaks of both GeSe and MoS₂. The peaks at 150.6 cm^{−1} and 187.4 cm^{−1}
21 represent the out-of-plane vibration mode (B_{3g}) and in-plane vibration mode (A_g) of
22 GeSe, respectively. The other two peaks at 383.5 cm^{−1} (in-plane vibration mode E^{1g}_{2g})
23 and 407.5 cm^{−1} (out-of-plane vibration mode A_{1g}) belong to MoS₂. The cross-section of
24 the heterojunction observed by TEM is displayed in **Fig. 1e**. The thickness of GeSe is
25 approximately 120 nm, and that of MoS₂ is approximately 6 nm. The GeSe nanoflake
26 is relatively thick for better light absorption, and the thin MoS₂ is chosen for the
27 effective collection of photo-generated electrons. A similar design has been reported in
28 BP/MoS₂ photodetectors.³² The vdW integration of GeSe and MoS₂ does not exhibit
29 mismatch or pinning on the interface, thus guaranteeing high electrical performance. In

1 this device, a thin amorphous layer is observed in the high-resolution image of the
2 GeSe/MoS₂ interface (**Fig. 1f**). This layer possibly originates from the exfoliation-
3 restack process, which may hinder the separation of photo-generated carriers and delay
4 the response time.³² The corresponding feature element maps obtained through energy-
5 dispersive X-ray spectroscopy (EDS) depict the spatial distribution of GeSe and MoS₂.
6

7 **Electrical properties and operation mechanism of the device**

8 As depicted in **Fig. 2a**, the device configuration consists of three functional parts
9 in a series-resistance mode: a p-type GeSe ferroelectric field-effect transistor (p-
10 FeFET), an n-type MoS₂ ferroelectric field-effect transistor (n-FeFET), and a
11 GeSe/MoS₂ Fe-VHJ. We can decide which one is dominant by changing the gate or
12 bias voltage. **Figure 2b** presents a micrograph of the device; the highlighted portion
13 represents the actual test area, corresponding to the three parts in **Fig. 2a**. From the
14 output curves in Supplementary Fig. 2, both MoS₂ and GeSe are well-contacted with
15 their electrodes, indicating that the Schottky barrier has little effect on the electrical
16 performance of the VHJ. The transfer characteristics of n-type MoS₂ and p-type GeSe
17 gated by P(VDF-TrFE) are portrayed in **Fig. 2c**, which shows the same hysteresis
18 direction. The transfer curve of MoS₂ exhibits ferroelectric hysteresis, whereas that of
19 GeSe does not. The counter-clockwise hysteresis of GeSe originates from charge
20 injection or carriers capture by traps sites. Due to the interface trap states, a large
21 hysteresis window is found in the transfer curve of a GeSe FET tuned by SiO₂ back
22 gate (Supplementary Fig. 3b). By contrast, under the modulation of P(VDF-TrFE) top
23 gate, part of the trap states is localized by the polarization field, thereby narrowing the
24 hysteresis window (Supplementary Fig. 3a). Furthermore, two peaks in gate current are
25 generated by polarization state reverse. So, the polarization electric field is indeed
26 applied to the channel. The ferroelectric electric field ($\sim 1.2 \times 10^9$ V/m) is giant
27 enough to modulate the intrinsic carrier concentration ($n_i \propto \exp(-E_g/2kT)$) and
28 broaden the spectral range as shown in Supplementary Fig. 4-5. Therefore, the P(VDF-
29 TrFE) is supposed to modulate band structure of GeSe. Detailed DFT calculations and

1 experimental analysis are provided in Supplementary Figs. 6-8 and Supplementary
2 Notes 1-2. The transfer characteristics of the VHJ gated by P(VDF-TrFE) are shown in
3 **Fig. 2d**. In the device configuration, the heterojunction is in series with MoS₂ and GeSe,
4 so the transfer characteristics of the device are also co-modulated by MoS₂ and GeSe
5 nano-flakes. The ferroelectric hysteresis is observed in the transfer curves at a forward
6 bias (1 V) and a reverse bias (-1 V). The transport plot can be sorted into two parts.
7 When V_{tg} sweeps from -40 V to 20 V and from -20 V to -40 V, P(VDF-TrFE) polymer
8 is polarized up (P_{up}) and MoS₂ channel is fully depleted, which turns off the entire
9 channel and results in the smallest I_d . When V_{tg} sweeps from 40 V to -20 V and from
10 20 V to 40 V, P(VDF-TrFE) polymer is polarized down (P_{down}), the MoS₂ channel is
11 turned on and most V_d loads on the p-type GeSe part. As a result, holes in GeSe domain
12 change the electrical properties of the channel and the drain current increases when the gate
13 voltage sweeps from 40 V to -20 V. Therefore, the carrier concentration of the Fe-VHJ
14 is modulated by polarization field, and the device can maintain two states without
15 external gate voltage. **Figure 2e** shows the output characteristics at three states: ‘Fresh’,
16 ‘ P_{up} ’, and ‘ P_{down} ’, corresponding to the different polarization states of P(VDF-TrFE).
17 At the Fresh state, the GeSe/MoS₂ junction acts as a *pn* diode, but its rectification ratio
18 is small. The ferroelectric polarization states have considerable impacts on reverse
19 current, whereas forward current remains almost unchanged. The changes in the reverse
20 current may result from the band structure transform at the heterojunction interface.

21 The experimental determination of band structures of semiconductors and
22 heterojunctions includes optical techniques^{26,33}, photoemission spectroscopy,^{26,34-36} and
23 electrical transport techniques^{37,38}. For the limitation of materials and device structure,
24 the photoemission, and optical techniques are not suitable for our device. Here, we
25 analyze the band structure evolution with polarization electric field from the electrical
26 transport properties and the phenomena model is built in **Fig. 2f-h**. At the fresh state,
27 GeSe and MoS₂ formed a type II heterojunction, which is conducive to photo-generated
28 carrier separation. According to Fig. 1b, the band offsets of the conduction bands and
29 the valence bands are 0.10 eV and 0.20 eV, respectively. In this GeSe/MoS₂ VHJ, the

difference between the Fermi level and the bottom of the valence band of GeSe is 0.27 eV, and the difference between the Fermi level and the top of the conduction band of MoS₂ is 0.38 eV. They are derived from the formulas: $n = (g_{2D}k_B T) \ln\{1 + \exp[-(E_F - E_C)/k_B T]\}$ and $p = (g_{2D}k_B T) \ln\{1 + \exp[-(E_F - E_V)/k_B T]\}$, where g_{2D} is 2D density of states in TMD semiconductor. The carrier density n and p are calculated by $n(p) = \sigma/\mu e$, where conductivity σ and mobility μ are extracted from the output and transfer curves in Supplementary Fig. 2. The calculation details are displayed in Supplementary Note 3. Consequently, the difference between the Fermi levels of these two materials can be calculated to be 0.35 eV before they contact. At P_{up} state, electrons in MoS₂ are depleted and the depletion region width of *pn* junction increases, resulting in suppression of reverse current. The dark current is approximately 0.2 nA, lower than that at the Fresh state. When P(VDF-TrFE) is polarized down, the downward polarization accumulates majority carriers in GeSe and MoS₂, leading to a narrower depletion region. Specifically, the bandgap reduction of GeSe changes the band alignment of the GeSe/MoS₂ heterojunction. Generally, an electrical field narrows the bandgap of semiconductors by shifting the conduction band minimum (CBM) downward while the conduction band maximum (VBM) is nearly a constant.^{25,39} Thus, the band structure evolution of GeSe changes the conduction band offset from 0.10 eV to a negative value, which derived from the temperature-dependent electrical properties in Supplementary Fig. 9. A type I (straddling) band alignment is formed at the P_{down} state, causing a small peak barrier in the heterojunction. Although the band offset ΔE_c is a small value, it has an effective impact on carrier transport. As shown in Supplementary Fig. 10, Fowler-Nordheim tunnelling occurs at the P_{down} state, indicating the existence of a triangle barrier on the conduction band. The peak on the conduction band is negligible under larger bias but restrict carriers transport under small reverse bias. Hereto, based on these electrical analyses, it is verified that the band alignment of the GeSe/MoS₂ can be effectively tuned by the ferroelectric field.

28

29 Performance of photovoltaic response

To characterise the photodetection performance of GeSe/MoS₂ Fe-VHJ, we tested its photoresponse from visible to near-infrared. To ensure a low and stable dark current, the P(VDF-TrFE) polymer is polarized up. As presented in **Fig. 3a**, the heterojunction demonstrates ultra-low dark current at $V_d = 0$ V and embraces highly sensitive photoresponse to 520 nm illumination with different incident light power. The I_d - V_d characteristics under different illumination intensities at P_{up} and P_{down} states are shown in **Fig. 3b** and **Fig. 3c**, respectively. The injection of photo-generated carriers makes the I_d - V_d curves shift, resulting in short-circuit current (I_{sc}) and open-circuit voltage (V_{oc}). The V_{oc} reaches 0.49 V at P_{up} state which is larger than 0.37 V of P_{down} state. The difference of V_{oc} indicates that the difference of Fermi levels is tuned by the electric field originated from ferroelectric polarization. Moreover, the dark current is suppressed at P_{up} state, leading to a larger photocurrent. Therefore, the Fe-VHJ shows a better photovoltaic response at P_{up} state, where GeSe/MoS₂ forms a type II band alignment. As shown in **Fig. 3d**, the photocurrent rise time is as short as 14 μ s and the fall time is 400 μ s. The defective interfacial layer between GeSe and MoS₂ makes a negative effect on the recombination of photo-generated carriers, causing such a slow fall time. Besides, traps in nonoverlapping regions of MoS₂ and GeSe are another factor limiting the response speed. I_{sc} and V_{oc} increased with the power of 520 nm light illumination, as indicated in **Fig. 3e**. When the device is saturated-absorption, they reach maximum values of 52 nA and 0.49 eV. **Figure 3f** shows the power-dependence of photoresponsivity (R) and detectivity (D^*) at $V_d = 0$ V. Photoresponsivity is calculated using the formula $R = I_{ph}/P$. Detectivity is calculated using $D^* = A^{1/2}R/(2eI_{dark})^{1/2}$, where A is the effective area of the photodetector (2×10^{-6} cm²), e is the elementary electronic charge, and I_{dark} is the dark current (1.5 pA). The photodetector achieves maximum photoresponsivity and detectivity values of 729.3 mA/W and 4.7×10^{13} Jones under the illumination of 520 nm light with 2.1 nW.

27

28 **Photoresponse in NIR of GeSe/MoS₂ Fe-VHJ**

1 In commercial integrated photonics based on Si or Ge, transceivers, modulators
2 and detectors operate at a wavelength between 1300 nm and 1550 nm (corresponding
3 $E_{\text{opt}} \approx 0.8$ eV).⁴⁰⁻⁴² According to the bandgaps of MoS₂ (1.2 eV) and GeSe (1.1 eV),
4 however, the application in integrated photonics of the GeSe/MoS₂ heterojunction is
5 spectrally limited. Nevertheless, the GeSe/MoS₂ Fe-VHJ is supposed to sensitive to
6 photons with lower energy because of the modulation of the giant ferroelectric field.
7 The transfer curves at $V_d = -1$ V with/without 1550 nm light illumination are plotted in
8 **Fig. 4a**. Photocurrents are generated when gate voltage sweeps from 0 V to 40 V and
9 40 V to -20 V, where GeSe plays a dominant role in the whole channel. A similar
10 response is observed in transfer curves at $V_d = 1$ V. Photocurrent maps confirm the
11 sensitivity of the whole GeSe area under near infrared irradiation (Supplementary Fig.
12 11), while only the overlapping heterojunction part shows sensitivity to visible light.
13 This indicates that the device operates in a photoconductive mode in the near-infrared
14 region. Additionally, the photocurrent switching characteristics under the illumination
15 of 1310 nm and 1550 nm are shown in **Fig. 4b** and **Fig. 4c**, respectively. The
16 GeSe/MoS₂ Fe-VHJ shows stable photocurrent switching characteristics at both reverse
17 and forward biases. In contrast to the response to visible light, the response to NIR light
18 with assistance of an external bias is much slower (see Supplementary Fig. 12) because
19 the type I band alignment is unfavorable to separate photo-generated carriers. The
20 energy band diagrams of GeSe/MoS₂ VHJ under various biases when P(VDF-TrFE) is
21 polarized down are shown in **Fig. 4d**. At equilibrium state, photo-generated carriers in
22 GeSe cannot overcome the peak in the conduction band, falling to be collected by
23 electrodes. With a reverse bias applied across the outer electrodes, the peak barrier is
24 covered by the steep band structure and no longer affects the transport of electrons.
25 Correspondingly, the band offset in the valence band is also negligible for collecting
26 photo-generated holes when a high enough forward bias is applied. As a result, the
27 photocurrent generated by infrared light can only be collected with large enough bias.
28 Therefore, band alignment evolution in GeSe/MoS₂ FeFET changes response mode

1 different from the photovoltaic effect in visible waveband, and the device operates in a
2 photoconductive mode in the near-infrared range.

3

4 **Polarization-resolved sensitivity of GeSe/MoS₂ Fe-VHJ**

5 Photodetectors are essential sensing tools for acquiring light information of the
6 environment. With the development of artificial intelligence, more accurate
7 information must be acquired and analysed. Anisotropic materials such as black
8 phosphorus (BP), ReS₂, ReSe₂, and GeSe have been successively employed to develop
9 polarization detectors.⁴³⁻⁴⁵ Among these materials, GeSe is a promising and rare *p*-type
10 semiconductor that can form ideal *pn* junctions with *n*-type 2D materials.^{31,46} More
11 importantly, GeSe has a direct bandgap for high-efficiency absorption.⁴⁷ As shown in
12 **Fig. 5**, the polarization-dependent photoresponse of the GeSe/MoS₂ Fe-VHJ is
13 comprehensively studied. The test setup is illustrated in **Fig. 5a**. The incident light was
14 emitted perpendicularly onto the device and polarized using a Glan–Taylor prism. By
15 rotating the half-wave plate, the polarization angle of the linearly polarized light was
16 altered, but the laser power remained stable. To determine the effective photoresponse
17 area, we performed photocurrent mapping on the device. Additionally, we measured
18 the fluctuation of photocurrent to different angles of incident light. The results are
19 presented in **Fig. 5b**. P(VDF-TrFE) maintains an upward polarization field during
20 scanning, and no bias is applied to the GeSe/MoS₂ heterojunction. 0° is set along with
21 the direction of a cleavage side of GeSe. The photocurrent mappings are successively
22 obtained from 0° to 90° by steps of 15°. The photocurrent intensity varies noticeably
23 with the incident polarization angle. The most significant photoresponse is achieved at
24 90° and the weakest at 0°. According to the device configuration, the response area is
25 the overlapping part of GeSe and MoS₂, indicating that these two materials formed an
26 effective *pn* junction. The specific relationship between photocurrent and polarization
27 angle must be discovered to quantitatively characterise the polarization sensitivity of
28 the device. **Figure 5c–f** show the relationship between the photocurrent and
29 polarization angle of the device from the visible to near-infrared wavelength (520 nm,

1 940 nm, 1060 nm, and 1310 nm), respectively. The photocurrent varies periodically
2 with the angle of incident polarized light. Fitting with the sine function $I_{\text{ph}}(\delta) = I_{\text{py}} \cos^2(\delta$
3 $+ \varphi) + I_{\text{px}} \sin^2(\delta + \varphi)$, the device dichroic ratio $I_{\text{py}}/I_{\text{px}}$ could be obtained to determine the
4 polarization detection capability of the device; the dichroic ratios of the device under
5 the illumination of 520 nm, 940 nm, 1060 nm, and 1310 nm are 5.53, 6.25, 3.80, and
6 3.16, respectively. These parameters are higher compared to GeSe photodetectors and
7 other anisotropic devices (shown in Supplementary Table 1).^{43,48,49} The enhancement
8 of the dichroism of GeSe, possibly originates from the anisotropic stark effect in
9 GeSe.⁵⁰ The GeSe/MoS₂ Fe-VHJ is a promising polarization-sensitive photodetector
10 for optical sensing.

11 **Conclusion**

12 In conclusion, we have designed a proof-of-concept device architecture, the
13 GeSe/MoS₂ Fe-VHJ. The carrier transport of the heterojunction can be effectively tuned
14 by the ferroelectric polarization field with band alignment evolution. The device
15 demonstrates quick and sensitive responsivity to visible incident light. Besides, the Fe-
16 VHJ is sensitive in the near-infrared region as well because of the band engineering of
17 ferroelectric dipoles. Ultimately, we used this single device to obtain the intensity and
18 polarization information of light. Our high-performance Fe-VHJ is a pioneering
19 integrated sensing device.

20

21 **Data availability**

22 The authors declare that the data that support the graphs within this paper are available
23 from the corresponding author upon reasonable request.

24

25 **References**

- 26 1. Matthews, J. *et al.* Defects in epitaxial multilayers: I. Misfit dislocations. *J. Cryst. Growth* **27**, 118-
27 125 (1974).
- 28 2. Matthews, J. *et al.* Defects in epitaxial multilayers: III. Preparation of almost perfect multilayers. *J.*
29 *Cryst. Growth* **32**, 265-273 (1976).
- 30 3. Vallet, M. *et al.* Highly strained AlAs-type interfaces in InAs/AlSb heterostructures. *Appl. Phys. Lett.*
31 **108**, 211908 (2016).

- 1 4. Qing Hua, W. *et al.* Electronics and optoelectronics of two-dimensional transition metal
2 dichalcogenides. *Nat. Nanotechnol.* **7**, 699-712 (2012).
- 3 5. Novoselov, K. S. *et al.* Electric field effect in atomically thin carbon films. *Science* **306**, 666-669
4 (2004).
- 5 6. Ferrari, A. C. *et al.* Raman spectrum of graphene and graphene layers. *Phys. Rev. Lett.* **97**, 187401
6 (2006).
- 7 7. Seyler, K. L. *et al.* Signatures of moire-trapped valley excitons in MoSe₂/WSe₂ heterobilayers. *Nature*
8 **567**, 66-70 (2019).
- 9 8. Liu, Y. *et al.* Van der Waals integration before and beyond two-dimensional materials. *Nature* **567**,
10 323-333 (2019).
- 11 9. Cao, Y. *et al.* Unconventional superconductivity in magic-angle graphene superlattices. *Nature* **556**,
12 43-50 (2018).
- 13 10. Cao, Y. *et al.* Correlated insulator behaviour at half-filling in magic-angle graphene superlattices.
14 *Nature* **556**, 80-84 (2018).
- 15 11. Furchi, M. M. *et al.* Photovoltaic effect in an electrically tunable van der Waals heterojunction. *Nano*
16 *Lett.* **14**, 4785-4791 (2014).
- 17 12. Woo Jong, Y. *et al.* Highly efficient gate-tunable photocurrent generation in vertical heterostructures
18 of layered materials. *Nat. Nanotechnol.* **8**, 952-958 (2013).
- 19 13. Withers, F. *et al.* Light-emitting diodes by band-structure engineering in van der Waals
20 heterostructures. *Nat. Mater.* **14**, 301-306 (2015).
- 21 14. Li, D. *et al.* Two-dimensional non-volatile programmable p-n junctions. *Nat. Nanotechnol.* **12**, 901–
22 906 (2017).
- 23 15. Liu, C. *et al.* A semi-floating gate memory based on van der Waals heterostructures for quasi-non-
24 volatile applications. *Nat. Nanotechnol.* **13**, 404-410 (2018).
- 25 16. Britnell, L. *et al.* Resonant tunnelling and negative differential conductance in graphene transistors.
26 *Nat. Commun.* **4**, 1794 (2013).
- 27 17. Yan, R. *et al.* Esaki diodes in van der Waals heterojunctions with broken-gap energy band alignment.
28 *Nano Lett.* **15**, 5791-5798 (2015).
- 29 18. Shim, J. *et al.* Phosphorene/Rhenium disulfide heterojunction-based negative differential resistance
30 device for multi-valued logic. *Nat. Commun.* **7**, 13413 (2016).
- 31 19. Li, D. *et al.* Gate-Controlled BP-WSe₂ Heterojunction Diode for Logic Rectifiers and Logic
32 Optoelectronics. *Small* **13**, 1603726 (2017).
- 33 20. Huang, M. *et al.* Multifunctional high-performance van der Waals heterostructures. *Nat. Nanotechnol.*
34 **12**, 1148-1154 (2017).
- 35 21. Ko, C. *et al.* Ferroelectrically Gated Atomically Thin Transition-Metal Dichalcogenides as
36 Nonvolatile Memory. *Adv. Mater.* **28**, 2923-2930 (2016).
- 37 22. Wu, G. *et al.* Programmable transition metal dichalcogenide homojunctions controlled by nonvolatile
38 ferroelectric domains. *Nat. Electron.* **3**, 43-50 (2020).
- 39 23. Wang, X. *et al.* Ultrasensitive and Broadband MoS₂ Photodetector Driven by Ferroelectrics. *Adv.*
40 *Mater.* **27**, 6575-6581 (2015).
- 41 24. Liu, Y. *et al.* Gate-Tunable Giant Stark Effect in Few-Layer Black Phosphorus. *Nano Lett.* **17**, 1970-
42 1977 (2017).
- 43 25. Deng, B. *et al.* Efficient electrical control of thin-film black phosphorus bandgap. *Nat. Commun.* **8**,
44 14474 (2017).

- 1 26. Chu, T. *et al.* Electrically Tunable Bandgaps in Bilayer MoS₂. *Nano Lett.* **15**, 8000-8007 (2015).
- 2 27. Zibouche, N. *et al.* Transition-metal dichalcogenide bilayers: Switching materials for spintronic and
3 valleytronic applications. *Phys. Rev. B* **90** (2014).
- 4 28. Si, M. *et al.* A ferroelectric semiconductor field-effect transistor. *Nat. Electron.* **2**, 580-586 (2019).
- 5 29. Ni, K. *et al.* Ferroelectric ternary content-addressable memory for one-shot learning. *Nat. Electron.*
6 **2**, 521-529 (2019).
- 7 30. Chen, Y. *et al.* Optoelectronic properties of few-layer MoS₂ FET gated by ferroelectric relaxor
8 polymer. *ACS Appl. Mater. Interfaces* **8**, 32083-32088 (2016).
- 9 31. Yap, W. C. *et al.* Layered material GeSe and vertical GeSe/MoS₂ p-n heterojunctions. *Nano Res.* **11**,
10 420-430 (2017).
- 11 32. Bullock, J. *et al.* Polarization-resolved black phosphorus/molybdenum disulfide mid-wave infrared
12 photodiodes with high detectivity at room temperature. *Nat. Photon.* **12**, 601-607 (2018).
- 13 33. Ubrig, N. *et al.* Design of van der Waals interfaces for broad-spectrum optoelectronics. *Nat. Mater.*
14 **19**, 299-304 (2020).
- 15 34. Wilson, N. R. Determination of band offsets, hybridization, and exciton binding in 2D semiconductor
16 heterostructures. *Sci. Adv.*, 1601832 (2017).
- 17 35. Pierucci, D. *et al.* Band Alignment and Minigaps in Monolayer MoS₂-Graphene van der Waals
18 Heterostructures. *Nano Lett.* **16**, 4054-4061 (2016).
- 19 36. Chiu, M. H. *et al.* Determination of band alignment in the single-layer MoS₂/WSe₂ heterojunction.
20 *Nat. Commun.* **6**, 6 (2015).
- 21 37. Xu, Y. *et al.* Contacts between Two- and Three-Dimensional Materials: Ohmic, Schottky, and p-n
22 Heterojunctions. *ACS Nano* **10**, 4895-4919 (2016).
- 23 38. Chen, X. *et al.* Widely tunable black phosphorus mid-infrared photodetector. *Nat. Commun.* **8**, 1672
24 (2017).
- 25 39. Qiu, Z. *et al.* Giant gate-tunable bandgap renormalization and excitonic effects in a 2D semiconductor.
26 *Sci. Adv.* **5**, 2347 (2019).
- 27 40. Romagnoli, M. *et al.* Graphene-based integrated photonics for next-generation datacom and telecom.
28 *Nat. Rev. Mater.* **3**, 392-414 (2018).
- 29 41. Bie, Y. Q. *et al.* A MoTe₂-based light-emitting diode and photodetector for silicon photonic integrated
30 circuits. *Nat. Nanotechnol.* **12**, 1124-1129 (2017).
- 31 42. Dumas, D. C. S. *et al.* Ge/SiGe quantum confined Stark effect electro-absorption modulation with
32 low voltage swing at $\lambda = 1550$ nm. *Opt. Express* **22**, 19284-19292 (2014).
- 33 43. Liu, F. *et al.* Highly sensitive detection of polarized light using anisotropic 2D ReS₂. *Adv. Func. Mater.*
34 **26**, 1169-1177 (2016).
- 35 44. Wang, X. *et al.* Short-wave near-infrared linear dichroism of two-dimensional Germanium Selenide.
36 *J. Am. Chem. Soc.* **139**, 14976-14982 (2017).
- 37 45. Shi, G. Anisotropic spin transport and strong visible-light absorbance in few-layer SnSe and GeSe.
38 *Nano lett.* **15**, 6926-6931 (2015).
- 39 46. Xue, D. J. *et al.* GeSe Thin-film solar cells fabricated by self-regulated rapid thermal sublimation. *J.*
40 *Am. Chem. Soc.* **139**, 958-965 (2017).
- 41 47. Xu, Y. *et al.* First-principles study on the electronic, optical, and transport properties of monolayer α -
42 and β -GeSe. *Phys. Rev. B* **96** (2017).
- 43 48. Ye, L. *et al.* Highly polarization sensitive infrared photodetector based on black phosphorus-on-WSe₂
44 photogate vertical heterostructure. *Nano Energy* **37**, 53-60 (2017).

1 49. Li, X. K. *et al.* Polarization-Dependent Photocurrent of Black Phosphorus/Rhenium Disulfide
2 Heterojunctions. *Adv. Mater. Interfaces* **5** (2018).

3 50. Kim, J. *et al.* Observation of tunable band gap and anisotropic Dirac semimetal state in black
4 phosphorus. *Science* **349**, 723-726 (2015).

5

6

1 **Acknowledgements**

2 This work is supported by the Strategic Priority Research Program of Chinese Academy
3 of Sciences (Grant No. XDB44000000 and XDB30000000), the Key Research Project
4 of Frontier Sciences of Chinese Academy of Sciences (QYZDB-SSW-JSC016,
5 QYZDY-SSW-JSC042, and QYZDB-SSW-JSC031), the Key Research Program of
6 Frontier Sciences, CAS (ZDBS-LY-JSC045), National Postdoctoral Program for
7 Innovative Talents (BX20180329), and the Natural Science Foundation of China (Grant
8 Nos. 61835012, 61905267, 61974153, 62004204, 62075228, 61622406, 61725505,
9 61674157 and 61734003).

10

11

12 **Author contributions**

13 Y.C and X.-D.W contributed equally to the work. J.W. and Y.C conceived the idea for
14 the project and designed the experiments. J.W. supervised the project. Z.-M.W. and X.-
15 T.W. synthesized the GeSe crystal. Y.C. and X.-D.W. fabricated devices and performed
16 electrical measurements. Y.C., W.H., Z.W., W.J, F.W, P.W, Y.J. and B.W. performed
17 optical measurement. H.L and Z.-M.W. carried out the calculated part. Y.C., X.-D.W.,
18 T.L., H.S., W.H., X.M. and J.C. analyzed the data. J.W., Y.C and X.-D.W. co-wrote
19 the manuscript. All authors discussed the results and commented on the manuscript.

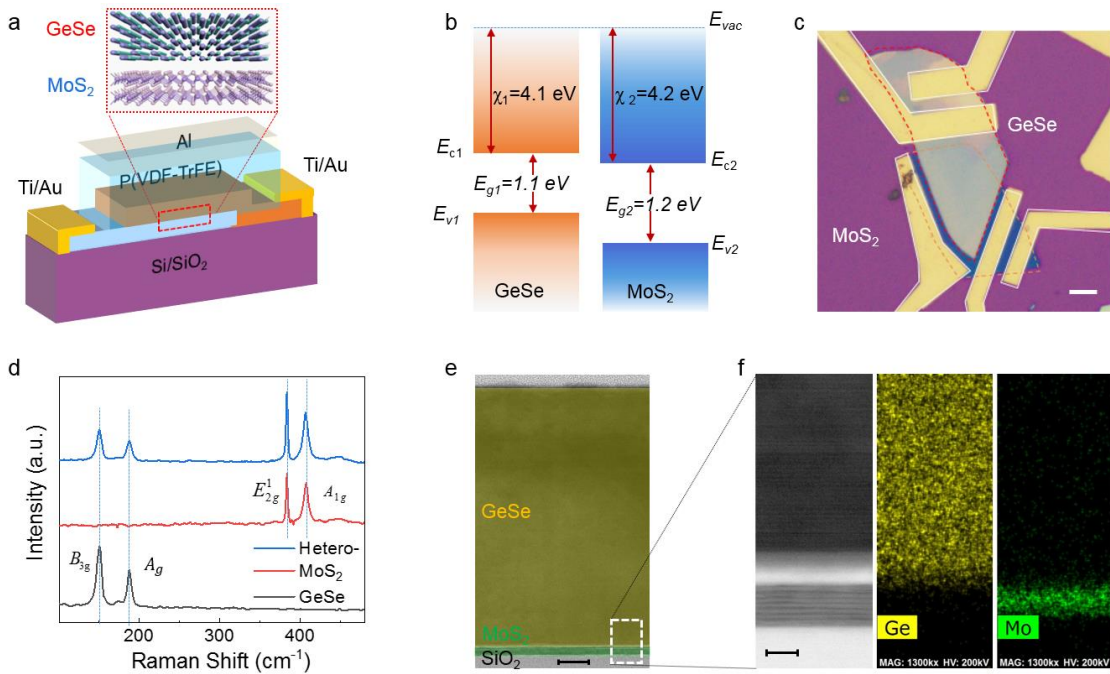
20

21 **Competing interests**

22 The authors declare no competing interests.

23

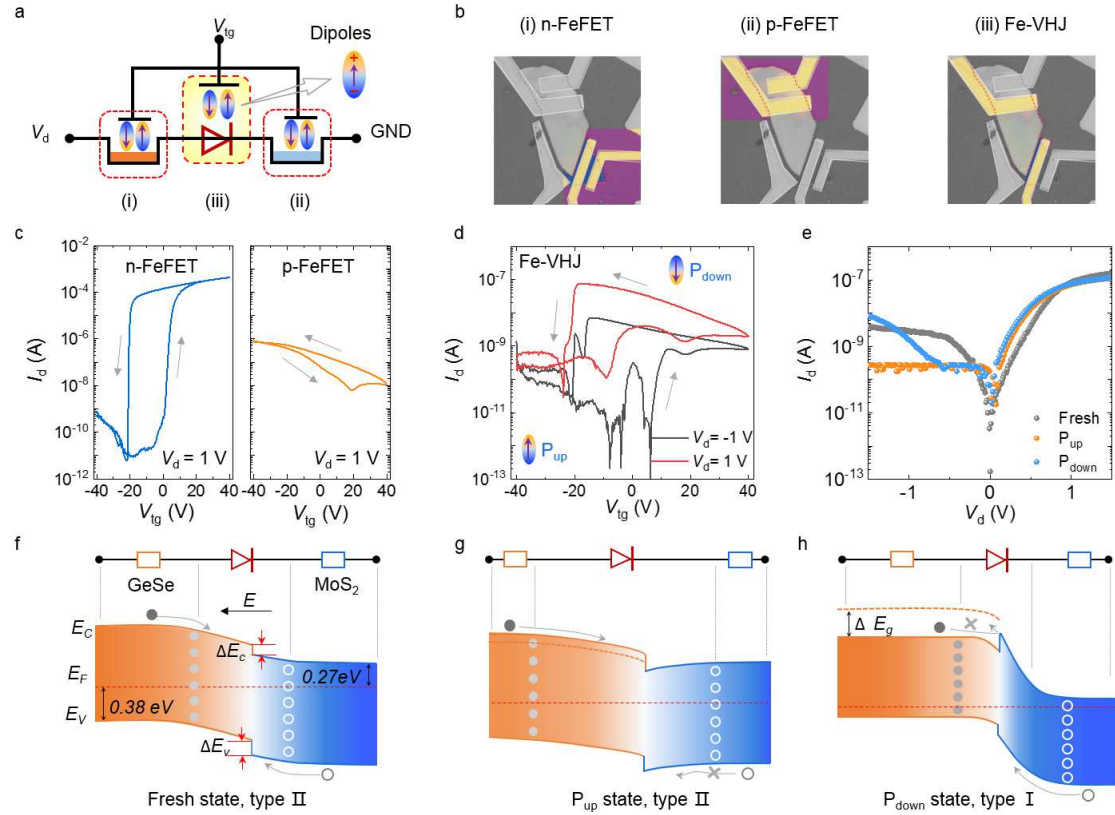
1



2

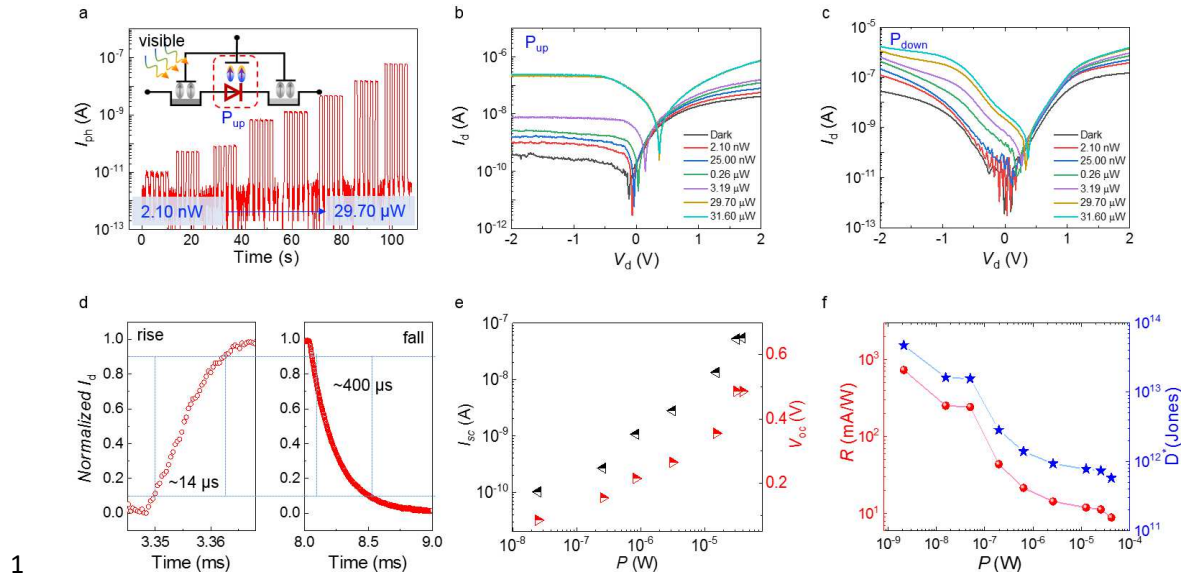
3 Figure 1 Design and characterization of GeSe/MoS₂ heterojunction. a, Schematic
4 illustration of the GeSe/MoS₂ heterojunction with the P(VDF-TrFE) gate. **b,** Energy
5 bands of GeSe and MoS₂ before contact. χ_1 , χ_2 , E_{g1} , and E_{g2} are from related literatures.
6 **c,** Optical micrograph of the heterojunction; scale bar: 5 μm. **d,** Raman spectra of GeSe
7 and MoS₂ and their overlap. **e,** TEM image of the heterostructure; scale bar: 10 nm. **f,**
8 High-resolution cross-sectional image of the GeSe/MoS₂ interface and the
9 corresponding chemical element distribution; scale bar: 5 nm.

10



1 **Figure 2 Electrical properties of GeSe/MoS₂ heterojunction tuned by the**
 2 **ferroelectric polymer P(VDF-TrFE).** **a**, Electrical configuration of the device, with
 3 three parts represented in the dashed-line frames. **b**, Optical image of three device
 4 elements: (i) MoS₂ n-FeFET, GeSe p-FeFET, and GeSe/MoS₂ Fe-VHJ. **c**, Transfer
 5 characteristics of GeSe p-FeFET and MoS₂ n-FeFET at $V_d = 1$ V. **d**, Transfer
 6 characteristics of the Fe-VHJ under forward and reverse biases. **e**, Output
 7 characteristics of the GeSe/MoS₂ heterojunction when P(VDF-TrFE) are fresh,
 8 polarized upward, and polarized downward states. **f**, Schematic of the energy band
 9 structure of the GeSe/MoS₂ junction at 'Fresh' state. E_F-E_C and E_F-E_V were calculated
 10 using experimental data. Schematic of the heterojunction energy bands at an
 11 equilibrium state. Bandgap evolution of the GeSe/MoS₂ Fe-VHJ at **g**, ' P_{up} ' state and **h**,
 12 ' P_{down} ' state.
 13

14



1 **Figure 3 Photoresponse performance of GeSe/MoS₂ Fe-VHJ in the visible region.**

2 **a**, Time-resolved photocurrent in the ‘P_{up}’ state with 520 nm incident light and power
3 are 2.10 nW, 25.00 nW, 50.10 nW, 0.26 μ W, 0.85 μ W, 3.19 μ W, 15.30 μ W, and 29.70
4 μ W, respectively. Output characteristics under different light powers at **b**, ‘P_{up}’ state
5 and **c**, ‘P_{down}’ state. **d**, 10%–90% photocurrent rise and decay times derived with $\lambda = 520$
6 nm illumination. **e**, Power dependency of short-circuit current and open-circuit voltage
7 with an incident light wavelength of 520 nm. **f**, Photoresponsivity and detectivity of
8 GeSe/MoS₂ Fe-VHJ.

9

10

11

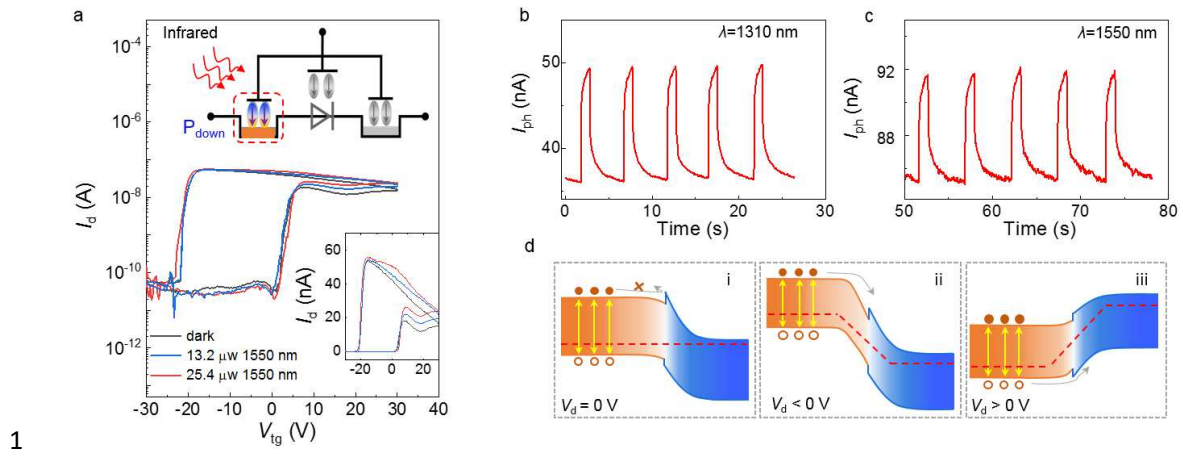


Figure 4 Photoresponse in near-infrared spectroscopy. **a**, Transfer curves under the illumination of 1550 nm light at $V_d = 1 \text{ V}$. Time-resolved photocurrent with incident light wavelengths of **b**, 1310 nm (P_{down} state, $V_d = -1 \text{ V}$) and **c**, 1550 nm (P_{down} state, $V_d = 1 \text{ V}$). **d**, Transport of the carriers generated by infrared light in GeSe/MoS₂ Fe-VHJ at (i) equilibrium state, (ii) reverse bias and (iii) forward bias.

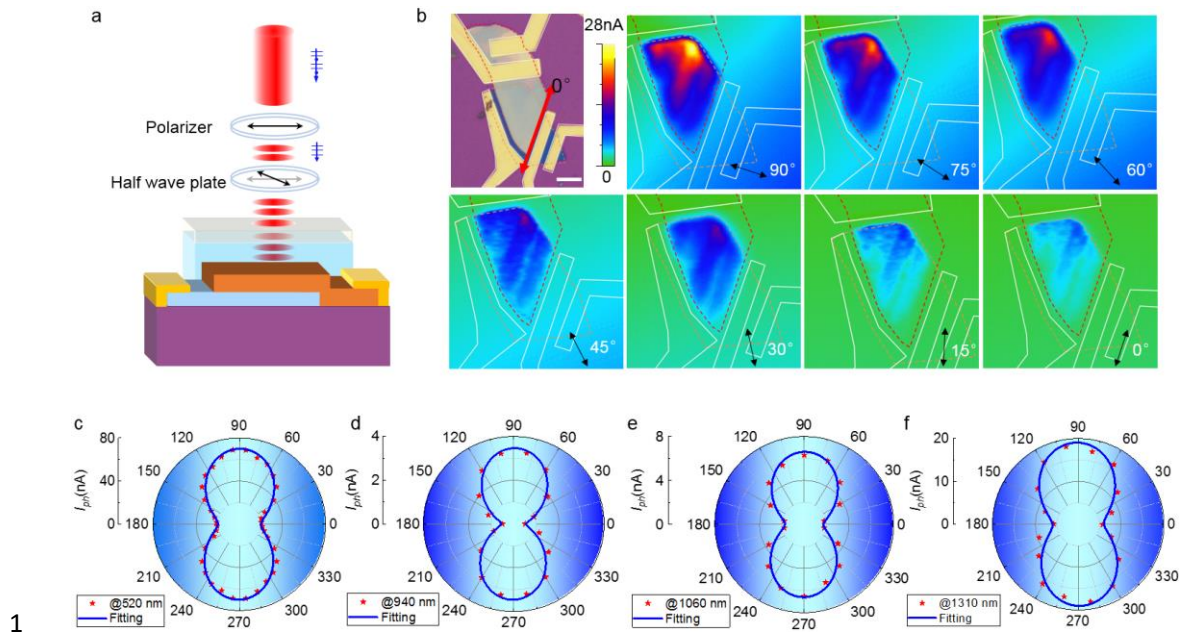


Figure 5 Polarization detection characteristics of the GeSe/MoS₂ Fe-VHJ. **a**, Schematic of the test setup. **b**, Photocurrent mapping of the GeSe/MoS₂ Fe-VHJ. **c–f**, Photocurrent as a function of the incident light polarization angle. The wavelength ranges from visible to near-infrared wavelengths (520 nm, 940 nm, 1060 nm, and 1310 nm). The solid line represents fitting using a sinusoidal function $I_{\text{ph}}(\delta) = I_{\text{py}} \cos^2(\delta + \varphi) + I_{\text{px}} \sin^2(\delta + \varphi)$. The fitted dichroic ratios under different wavelengths are 5.53, 6.25, 3.80, and 3.16.

Figures

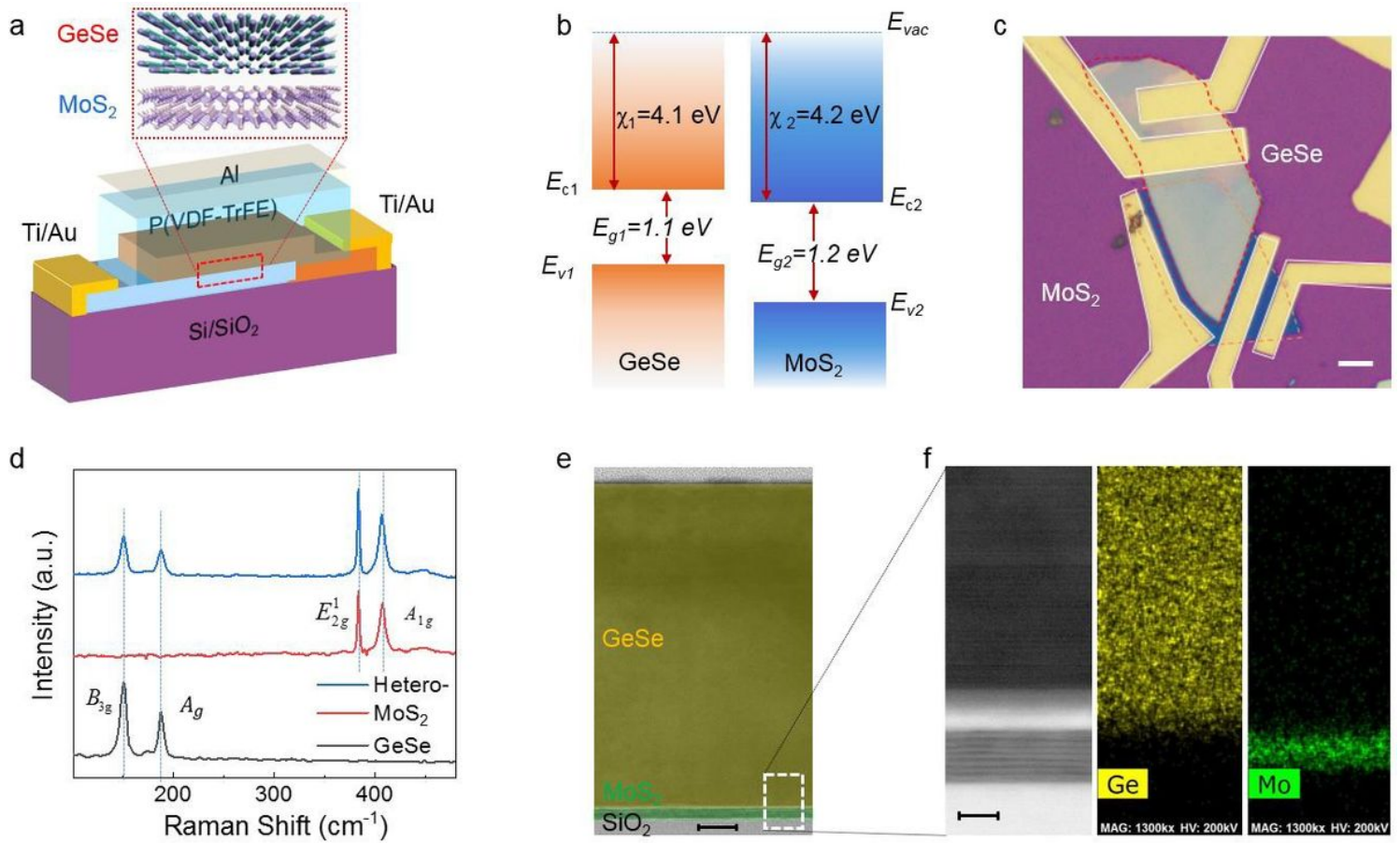


Figure 1

Design and characterization of GeSe/MoS₂ heterojunction. a, Schematic illustration of the GeSe/MoS₂ heterojunction with the P(VDF-TrFE) gate. b, Energy bands of GeSe and MoS₂ before contact. $\chi_1 \otimes \chi_2 \otimes E_g 1$, and $E_g 1$ are from related literatures. 5 c, Optical micrograph of the heterojunction; scale bar: μm . d, Raman spectra of GeSe and MoS₂ and their overlap. e, TEM image of the heterostructure; scale bar: 10 nm. f, High-resolution cross-sectional image of the GeSe/MoS₂ interface and the corresponding chemical element distribution; scale bar: 5 nm.

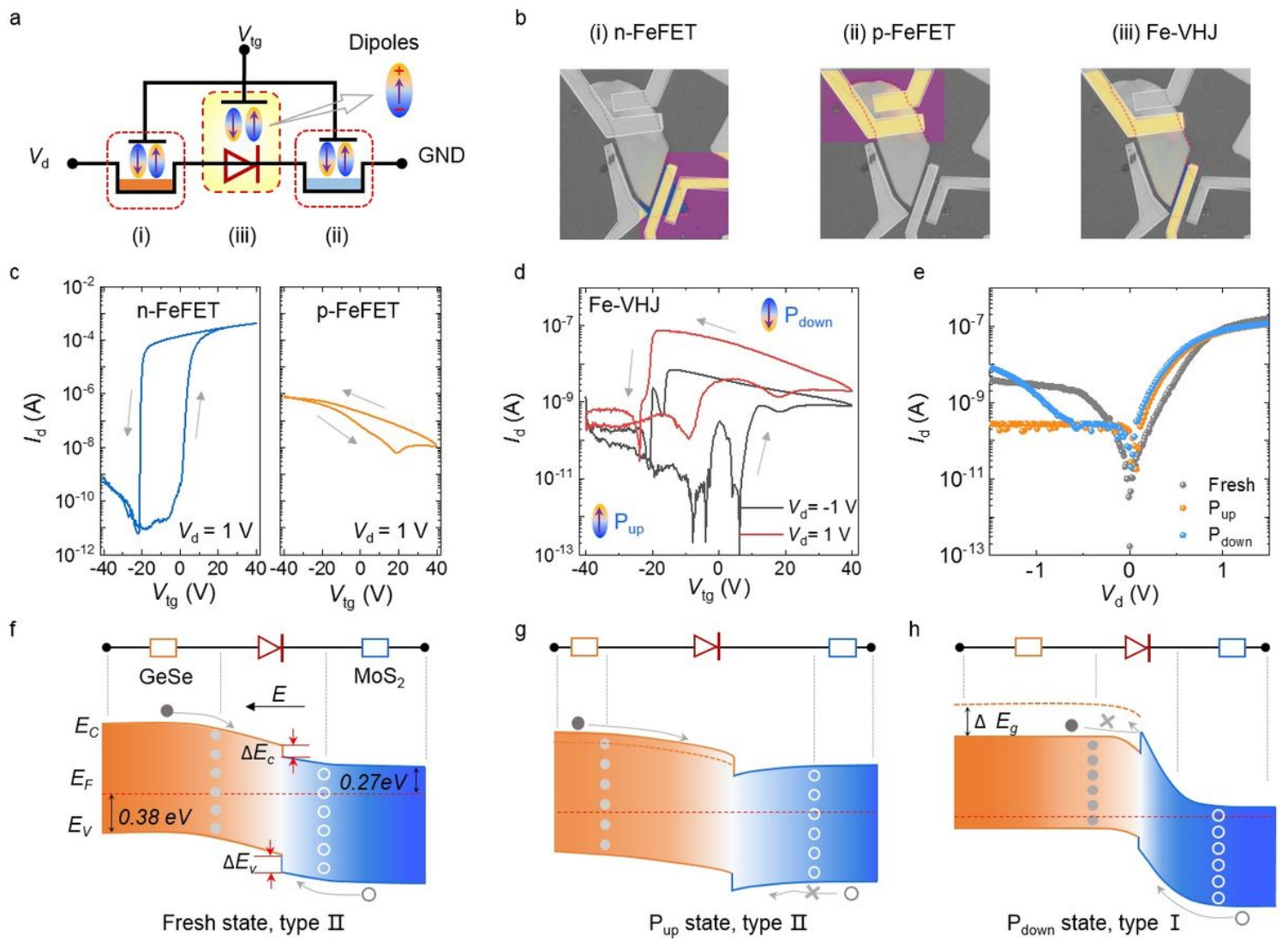


Figure 2

Electrical properties of GeSe/MoS₂ heterojunction tuned by the ferroelectric polymer P(VDF-TrFE). a, Electrical configuration of the device, with three parts represented in the dashed-line frames. b, Optical image of three device elements: (i) MoS₂ n-FeFET, GeSe p-FeFET, and GeSe/MoS₂ Fe-VHJ. c, Transfer characteristics of GeSe p-FeFET and MoS₂ n-FeFET at $V_d = 1$ V. d, Transfer characteristics of the Fe-VHJ under forward and reverse biases. e, Output characteristics of the GeSe/MoS₂ heterojunction when P(VDF-TrFE) are fresh, polarized upward, and polarized downward states. f, Schematic of the energy band structure of the GeSe/MoS₂ junction at ‘Fresh’ state. EF-EC and EF-E_V were calculated using experimental data. Schematic of the heterojunction energy bands at an equilibrium state. Bandgap evolution of the GeSe/MoS₂ Fe-VHJ at g, ‘Pup’ state and h, ‘Pdown’ state.

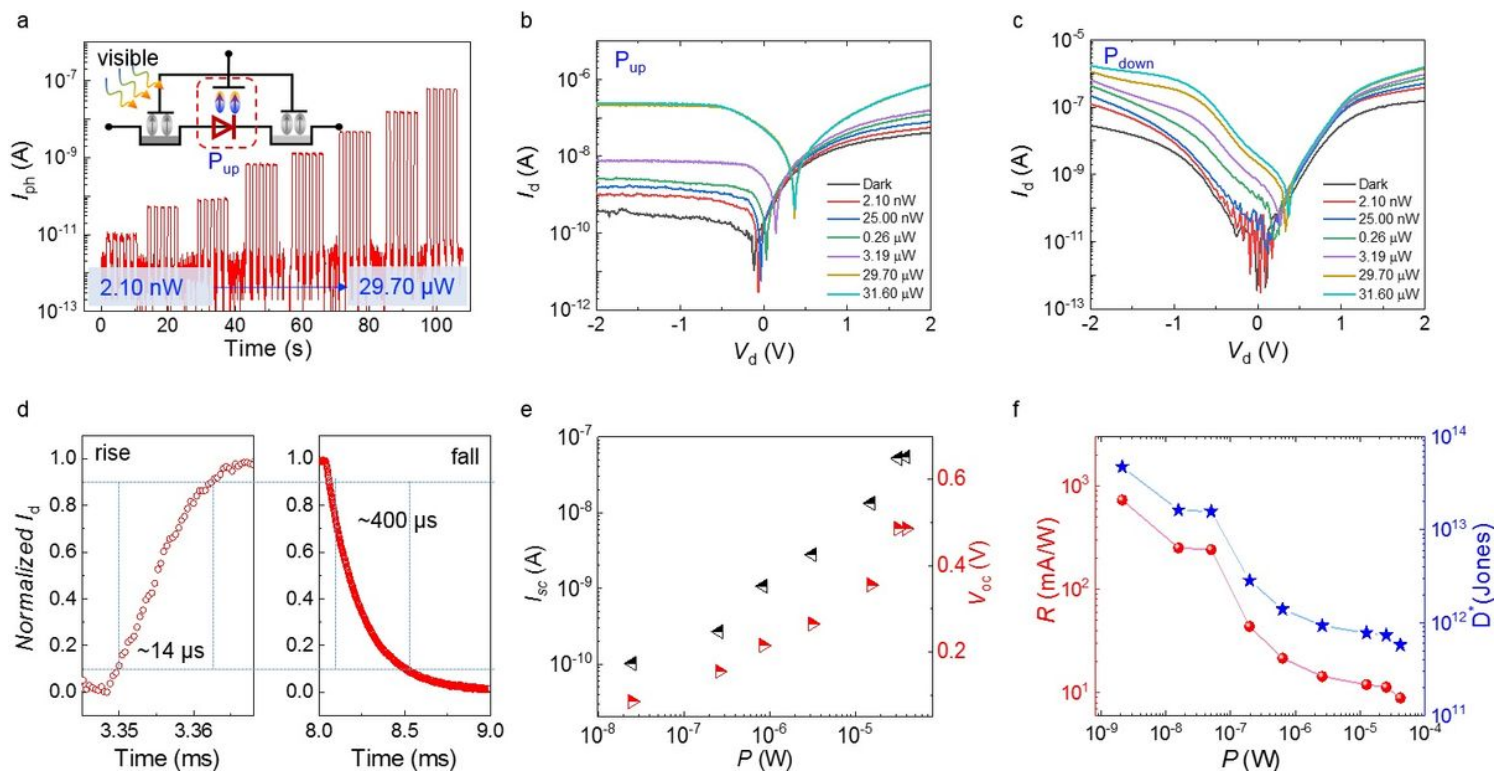


Figure 3

Photoresponse performance of GeSe/MoS₂ Fe-VHJ in the visible region. a, Time-resolved photocurrent in the ‘Pup’ state with 520 nm incident light and power are 2.10 nW, 25.00 nW, 50.10 nW, 0.26 uW, 0.85 uW, 3.19 uW, 15.30 uW, and 29.70 uW, respectively. Output characteristics under different light powers at b, ‘Pup’ state and c, ‘Pdown’ state. d, 10%–90% photocurrent rise and decay times derived with $\lambda = 520$ nm illumination. e, Power dependency of short-circuit current and open-circuit voltage with an incident light wavelength of 520 nm. f, Photoresponsivity and detectivity of GeSe/MoS₂ Fe-VHJ.

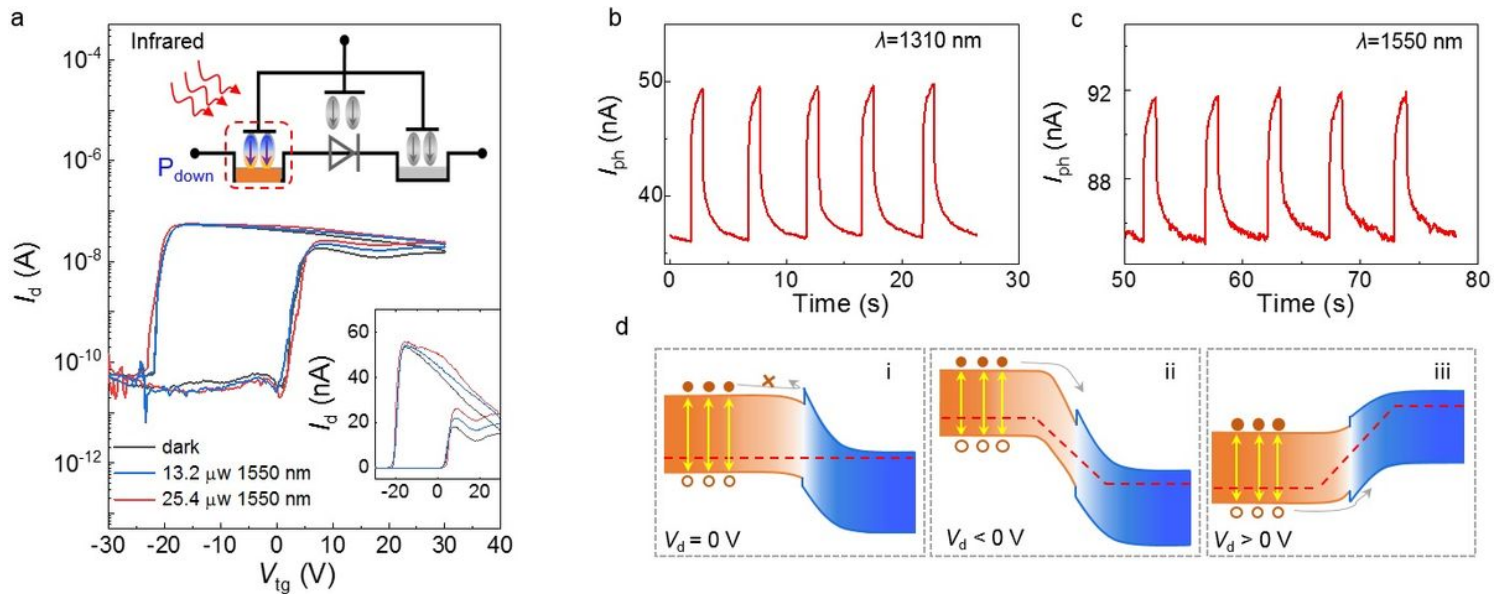


Figure 4

Photoresponse in near-infrared spectroscopy. a, Transfer curves under the illumination of 1550 nm light at $V_d = 1$ V. Time-resolved photocurrent with incident light wavelengths of b, 1310 nm (Pdown state, $V_d = -1$ V) and c, 1550 nm (Pdown state, $V_d = 1$ V). d, Transport of the carriers generated by infrared light in GeSe/MoS₂ Fe-VHJ at (i) equilibrium state, (ii) reverse bias and (iii) forward bias.

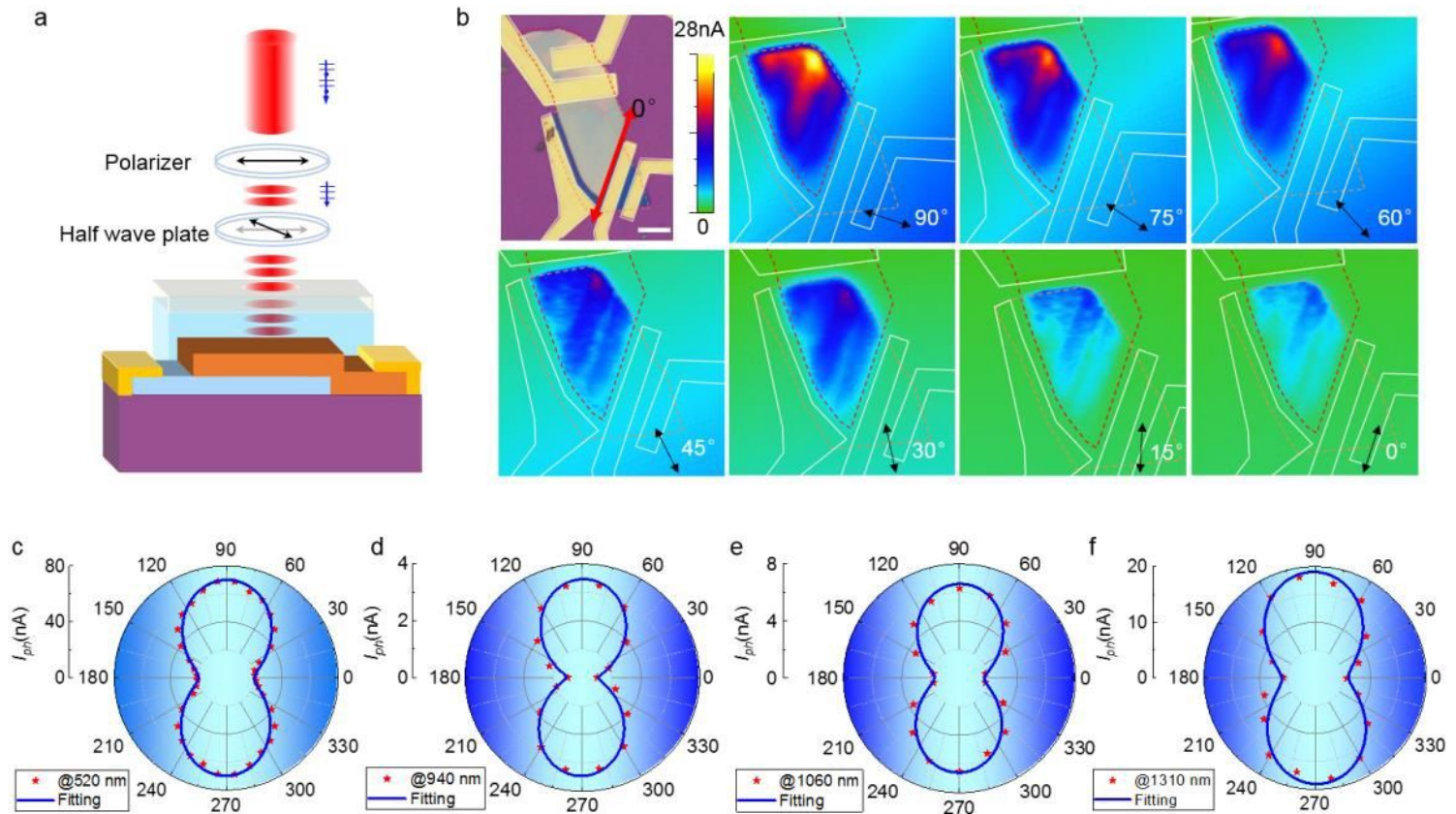


Figure 5

Polarization detection characteristics of the GeSe/MoS₂ Fe-VHJ. a, Schematic of the test setup. b, Photocurrent mapping of the GeSe/MoS₂ Fe-VHJ. c–f, Photocurrent as a function of the incident light polarization angle. The wavelength ranges from visible to near-infrared wavelengths (520 nm, 940 nm, 1060 nm, and 1310 nm). The solid line represents fitting using a sinusoidal function $I_{ph}(\delta) = I_{py} \cos^2(\delta + \varphi) + I_{px} \sin^2(\delta + \varphi)$. The fitted dichroic ratios under different wavelengths are 5.53, 6.25, 7.380, and 3.16.

Supplementary Files

This is a list of supplementary files associated with this preprint. Click to download.

- [SupplementaryInformation1222.docx](#)